



## Research Article

<https://doi.org/10.1631/jzus.A2500549>

# An adaptive adjustment strategy for EPB operation parameters for precontrol of shield tunneling-induced surface settlement: a case study

Dongsheng WEI, Haibin WEI, Zipeng MA<sup>✉</sup>, Heting WEI, Lijie SUN, Xiaokun YU

*College of transportation, Jilin University, Changchun 130022, China*

**Abstract:** During shield tunneling, ground deformation poses significant safety risks. The full optimization strategy ignores interactions between parameters, resulting in suboptimal performance in the precontrol of settlement in earth pressure balance shields. To address this problem, this paper proposes an integrated strategy that combines optimization and inversion, minimizing parameter interaction interference through adaptive adjustment of shield operation parameters. This mechanism performs an optimization search on the key operation parameters for settlement control, while the remaining operation parameters are predicted through inversion. Taking the Changchun Metro Line 6 project as an example, a bidirectional long short-term memory model enhanced by a multihead self-attention mechanism is used to predict shield tunneling-induced settlement with spatiotemporal sequence dependency relationships. Particle swarm optimization and a random forest algorithm are used for optimization and inversion operations in the integrated mechanism, respectively. Subsequent ring position tests showed that the integrated mechanism-based adaptive adjustment strategy limited the average fluctuation of uncontrollable parameters to  $\pm 13.95\%$  compared to  $\pm 34.27\%$  for the full optimization strategy. The actual average settlement was only 3.81 mm compared to 4.72 mm for the full optimization strategy through collaborative parameter adjustment. The application validated the feasibility and applicability of the integrated mechanism, providing important references for the adaptive adjustment of shield parameters and tunnel construction automation.

**Key words:** Precontrol of settlement; Optimization and inversion; Multihead self-attention; Long short-term memory; Random forest algorithm

## 1 Introduction

The development of underground space effectively addresses the challenges associated with urban sprawl, with subway-led underground rail systems rapidly advancing (Xu and Chen, 2023). Shield tunneling, favored for its minimal disruption, efficiency, and cost-effectiveness, is extensively utilized in underground construction projects (Hou et al., 2022). However, the process presents risks such as groundwater influx and geological hazards, which are particularly concerning when tunnelling near existing

structures. Excessive settlement in these areas can damage buildings and underground utilities, significantly threatening public safety and property. Given these risks, controlling settlement during shield tunneling has become an urgent issue in current underground transportation construction, requiring the adoption of effective measures to limit surface settlements.

At present, conventional technical methods for controlling shield tunneling-induced surface settlement ( $S_s$ ) mainly involve adjusting shield operation parameters and grouting treatment inside and outside the tunnel based on on-site measured settlement data. However, the passive remediation measures taken after settlement exhibit hysteresis, potentially causing irreversible residual deformations and thereby posing safety risks to the utilization and functionality of sensitive buildings and structures. To predict settlements caused by shield tunneling, a

✉ Zipeng MA, mazp@jlu.edu.cn

Dongsheng WEI, <https://orcid.org/0000-0003-0789-4249>

Received Oct. 28, 2026; Revision accepted Apr. 22, 2026;  
Crosschecked

multitude of researchers have engaged in pertinent studies utilizing methods such as empirical formulas (Luo et al., 2020, Mair et al., 1993, Standing and Burland, 2006, Zhang et al., 2021b), analytical solutions and in situ predictions (Deng and Wang, 2013, Galera et al., 2007), and numerical simulations (Maleki, 2018, Zhang et al., 2020a). Concurrently, various strategies for estimating the optimal operation parameters of shield tunneling have been proposed. Due to the spatial variability of geological and geotechnical parameters, estimates based on empirical and analytical formulas are often not accurate enough, and numerical methods, which are time-consuming in model creation and computation, are not very feasible in the optimization of shield parameters that have strong real-time requirements.

With the development of computer science, digital twins, big data analysis and other technologies continue to develop and integrate increasingly closely in various industries. The innovative thinking of industrial integration has led to significant achievements in various fields. In civil engineering intelligent construction (CEIC), machine learning (ML) methods can find the mathematical relationship between various factors and the predicted target in a data-driven way and can obtain the predicted result in a short time, which makes ML play an important role in the field of surface settlement prediction caused by shield tunneling (Chen et al., 2022, Kong et al., 2022, Suwansawat and Einstein, 2006). When using an artificial neural network (ANN), a backpropagation neural network (BPNN) has been applied for the first time to predict  $S_s$ , which is acceptable despite the prediction error (Kim et al., 2001). To reduce the prediction error and minimize the risk of tunneling, Pourtaghi and Lotfollahi-Yaghin (2012) proposed an alternative method for predicting the maximum surface settlement based on the integration of wavelet theory and ANN. Currently, an increasing number of ML methods have been adopted, such as decision trees (DTs), LASSO regression, support vector regression (SVR) (Wei et al., 2023), random forests (RFs) (Zhang et al., 2020c), and gradient boosting decision trees (GBDTs) (Zhang et al., 2021a, Zhou et al., 2023a). Additionally, more scholars have combined ML with optimization algorithms to reduce errors in settlement prediction by reasonably optimizing models or processing variables (Shi et al.,

2021, Zhou et al., 2023b). It has been found that long short-term memory (LSTM) has stronger memory retention and selection ability (Al Mehedi et al., 2023, Li et al., 2022, Zhang et al., 2020b) and can consider the sequence effects of deformation and surface settlement caused by shield tunneling. Attention mechanisms, introduced in recent years, excel at learning spatiotemporal correlations between datasets by assigning attention weights to individual steps, demonstrating an outstanding ability to capture long-term dependencies between steps, key data information, and internal autocorrelations within the data. LSTM variants, e.g., CNN-SA-LSTM (Gao et al., 2024, Yang et al., 2025) and CNN-LSTM-Attention (Bao et al., 2025, Wang et al., 2025, Zhao et al., 2024), incorporate self-attention (SA) mechanisms, demonstrating significantly higher accuracy and handling sequential data well. Although the multihead self-attention (MHSA) mechanism is more effective than the SA mechanism in extracting richer data features from a multilevel perspective across various subspaces, there is limited research on integrating it within existing models to predict surface settlement caused by shield tunneling (Song et al., 2024). Therefore, in this study, the bidirectional LSTM (Bi-LSTM) model was selected as the baseline framework and integrated with the MHSA mechanism to form the MHSA-Bi-LSTM model to capture spatiotemporal correlations and extract key data features.

In practical engineering, the control of shield tunneling parameters mainly relies on manual experience, which is significantly subjective. Improper parameter adjustment has become the main cause of recent shield tunneling accidents. An increasing number of studies have shown that there is a close relationship between geotechnical parameters, tunneling parameters and settlement deformation in shield construction. Some scholars have carried out in-depth studies on the optimization of tunneling parameters to ensure that the shield can operate efficiently under the expected working conditions. Liu and Ding (2020), through sensitivity analysis, found that synchronous grouting pressure and advance speed are parameters affecting the support pressure, while cutter rotating speed, cutter torque, and actual excavation amount are parameters affecting the deviation angle. Close attention to and

adjustment of parameters with greater impact can thus optimize the tunnel excavation process. Lin et al. (2021) established a muck chamber support pressure prediction model based on a GA (genetic algorithm)-BPNN and proposed an optimization mechanism for tunneling parameters, which enables the prediction and control of support pressure. When the control of surface settlement is considered as a separate criterion, researchers (Hou et al., 2020, Sun, 2022) have put forward a similar approach, mainly finding the shield parameters by searching. Although this method can effectively reduce the computational complexity, the synergistic effect between some parameters, such as support pressure and cutter torque, is ignored and is jointly determined by controllable operation parameters and geometric and ground conditions, which leads to a discrepancy between theoretical results and actual operation, thus resulting in a lack of practical engineering value. In response, Zhang et al. (2019) proposed a method for optimizing shield operation parameters when settlement exceeds the allowable value, which involves preventing abnormal settlement through parameter adjustment. This method requires a clear division of superior and inferior subsets of samples, and inevitably, there will be some limitations in its application. Optimizing shield operation parameters to guide the shield work in the best configuration state still requires further in-depth research within the engineering field.

In light of the current state of affairs, this study introduces a mechanism that integrates an optimization and inversion algorithm. It is designed to achieve preemptive management of  $S_s$ , mitigating the interference of interdependencies among shield parameters. The MHSA-Bi-LSTM and RF methods are applied to the prediction of settlement with sequence relationships and the inversion prediction of operation parameters with limited monitoring accuracy, respectively. A partitioning strategy for operation parameters is proposed, thereby establishing a composite optimization mechanism. A case study is presented, demonstrating the practical implementation and effectiveness of the proposed method from the Changchun Metro Line 6 construction project. The proposed method uses settlement control as a separate judging criterion for constructing a recommendation system of operation

parameters to assist shield driving to promote advancement in the field of shield automation and a reduction in construction safety problems.

## 2 Methodology

### 2.1 Shield tunneling-induced surface settlement forecast model

Earth pressure balance (EPB) shields turn the excavated material into a soil paste by soil conditioning that is used as a pliable, plastic support medium. This makes it possible to balance the pressure conditions at the tunnel face, avoids uncontrolled inflow of soil into the machine and creates the conditions for rapid tunneling with minimum settlement (Herrenknecht, 2024). Fig. S1 shows a comprehensive schematic of key parameters and the shield tunneling process in EPB construction.

Since it is impossible to achieve single-variable control in actual shield tunneling, a unique relationship between surface settlement and various parameters cannot be determined, but the surface settlement is affected by multifactor coupling (Li et al., 2015). In computer simulation or ML studies, the main factors influencing surface settlement are categorized into geometrical parameters, geotechnical parameters, and shield operation parameters. The surface settlement caused by shield construction can be regarded as a spatiotemporal sequence prediction problem: the surface settlement at a particular moment (time) and at a particular location (space), for example, at the back of the completed excavation ring (space) (Ding et al., 2013, Richa et al., 2023). The preshield arrival surface settlement at a particular time is affected by factors such as the support pressure on the unreached section. Therefore, it is necessary to predict the surface settlement based on multifactor spatial sequence data.

In the context of tunnel engineering, the depth-to-span ratio (the ratio of cover depth to tunnel diameter) and the center-to-center distance of twin tunnels are recognized as critical geometric parameters that substantially influence surface settlement. However, tunnel dimensions are typically fixed in each individual engineering study. The twin tunnels in this project are nearly parallel, with a center-to-center distance ranging from 13 to 17 m. This distance satisfies the empirical criterion of being

greater than 2.0 times the tunnel diameter, which is widely recognized as a reasonable range to minimize interaction effects between adjacent tunnels and ensure construction safety (Ghaboussi and Ranken, 1977, Hage Chehade and Shahrour, 2008). Consequently, the cover depth ( $D_C$ ) is identified as the only geometric parameter for consideration.

Drawing on pertinent literature (Li et al., 2022, Zhang et al., 2020b), key mechanical parameters are identified as the constrained modulus ( $E_{oed}$ ), cohesion ( $c$ ), angle of internal friction ( $\phi$ ), and lateral earth pressure coefficient at rest ( $K_0$ ). During soil mechanics property experiments for this engineering project, minimal variation in the Poisson's ratio and void ratio of distinct soil strata was observed, suggesting that these parameters have a negligible influence on settlement. Studies (Huang et al., 2021, Wu et al., 2019) have highlighted the presence of groundwater seepage at the excavation face and the interface of the tail shield as contributing to the consolidation settlement of the soil. The elevation of the groundwater table not only indirectly regulates the rate of seepage but also influences the soil stability. Therefore, the water table level ( $L_w$ ) is selected as an important hydrogeological parameter.

Research has demonstrated that the majority of shield operation parameters, to varying degrees, can influence surface settlement. Nonetheless, an overabundance of input parameters with excessive dimensionality may lead to difficulties in model convergence. Thus, parameters that have direct or indirect interactions with the soil are prioritized. Accordingly, the selection of the volume of synchronous grouting ( $V_G$ ) (Niu et al., 2023), total thrust ( $T_T$ ), cutterhead torque ( $T_C$ ), cutterhead rotating speed ( $R_C$ ) (Wang et al., 2021), support pressure ( $P_S$ ), advance speed ( $S_A$ ) (Cheng et al., 2022), screw conveyor rotational speed ( $R_{SC}$ ), screw conveyor torque ( $T_{SC}$ ), and volume of excavated earth ( $V_E$ ) (Lv et al., 2020) are selected as the relevant shield operation parameters. Previous studies have identified that these parameters exert a significant influence on the stability of the excavation face and surface settlement (Hu et al., 2021).

Given the numerous unknown or assumed conditions, such as ground anisotropy, stress conditions and variable geotechnical parameters, it is difficult to accurately predict surface deformation by

conventional methods (Galera et al., 2007). To address this issue, preliminary monitoring of each location is essential. As shown in Fig. 1, the preshield arrival surface settlement ( $S_{PS}$ ) was used as a time input parameter, and  $S_S$  was mapped together with other influencing parameters.

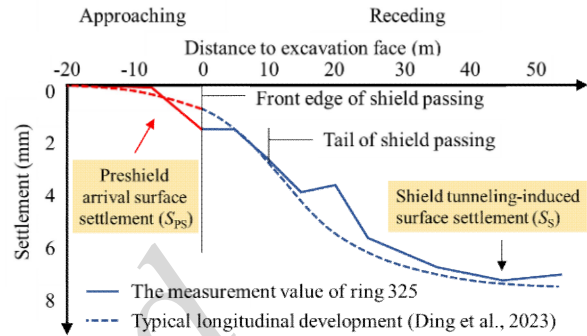


**Fig. 1 Schematic of longitudinal development (Ding et al., 2013) and parameter selection of surface settlement**

## 2.2 Strategy of adaptive adjustment

The EPB shield (model ZTE6250) has a reliable synchronized grouting, propulsion, measurement and grading system, which adjusts the grouting pressure and speed according to the real-time shield tail gap data and changes the advance speed and attitude by controlling the jacking thrust. In practical engineering applications, it is necessary to take into account the controllable nature and interactive synergies of parameters with the advance speed, cutter head rotation speed and screw conveyor rotational speed, i.e.,  $S_A$ ,  $R_C$  and  $R_{SC}$ , being directly determined by the operator, but with the total thrust, support pressure and cutterhead torque, i.e.,  $T_T$ ,  $P_S$  and  $T_C$ , and other parameters being jointly influenced by controllable parameters and geometric and ground conditions (Li et al., 2021, Wang et al., 2024). In addition, there are varying interaction effects between these parameters, as shown in Fig. S2, which is similar to the topology network structure.

While searching all parameters can yield the optimal outcome, doing so might disrupt the inherent interactive relationships between the parameters. To address this, by leveraging the distinctive advantages of ML methods in dealing with problems of high coupling among influencing factors and indeterminate reasoning rules, this paper introduces an innovative method that employs a combination of

optimization and inverse prediction strategies, minimizing the impact of the interaction between shield parameters. This methodology is designed to realize the self-adaptation of shield machinery, with

its summary illustrated in Fig. 2.

The entire procedure is bifurcated into Design Phase I and Construction Phase II.

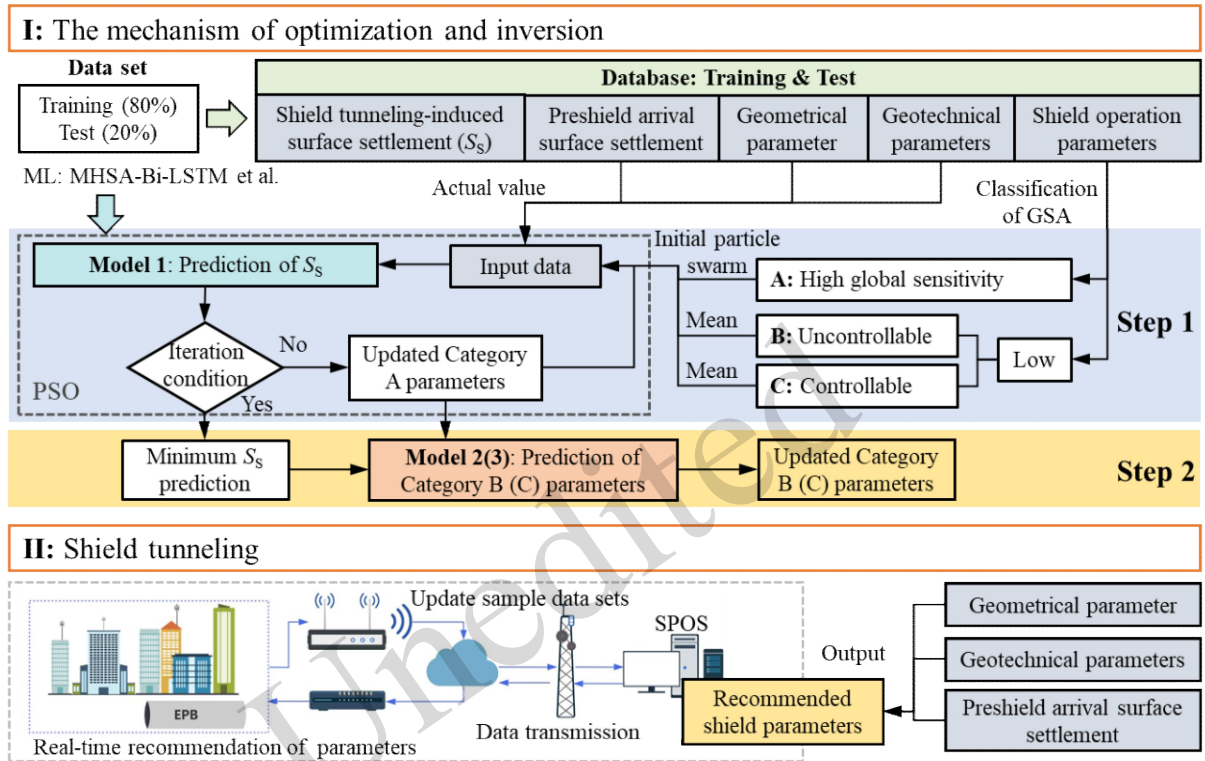


Fig. 2 Schematic diagram of the self-adaptation method of EPB shield tunneling

Phase I begins with the development of a shield tunneling settlement prediction model (Model 1), which is then utilized as a meta-model for conducting parameter sensitivity analyses and other operations. A multiclassification method for shield operation parameters is developed to target the control of settlement. Operation parameters with high global sensitivity are classified as Category A (high sensitivity) parameters, and those with low global sensitivity are classified as Category B (low sensitivity uncontrollable) and C (low sensitivity controllable) parameters according to whether they are artificially regulated. The first step in the adaptive adjustment mechanism involves recommendations for Category A parameters, which determine the settlement through an integration of the settlement prediction model with the particle swarm operation (PSO) algorithm. In contrast, Category B and C parameters, which possess low global sensitivity, are initialized with their respective mean values as model

inputs. In the second step, as illustrated in Fig. 3 (which presents a detailed view of the inversion prediction module in step 2 of Fig. 2.), the updated Category A parameters, in tandem with geometric and geotechnical parameters and settlements, are used to inversely derive new Category B parameters through Model 2. This is followed by the inverse prediction of Category C parameters through Model 3 and all the aforementioned parameters, which makes it possible to recommend human-controllable parameters more precisely by adding input parameter dimensions. At this point, the entire optimization workflow is complete. This strategy optimizes resources by focusing on parameters that play a dominant role in settlement, significantly reducing computational complexity. At the same time, it maximizes the retention of parameter interactions, avoids the optimization bias caused by traditional methods that ignore parameter correlations, and more accurately reflects the impact of parameter synergies on

tunneling-induced settlement.

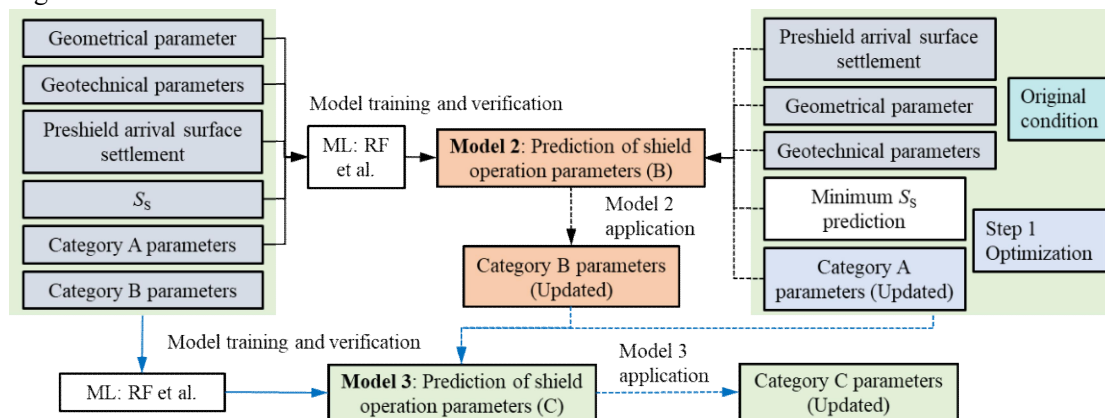


Fig. 3 Inversion prediction of Category B and C shield operation parameters

Phase II is dedicated to developing the Shield parameter optimization system (SPOS), as shown in Fig. S3, for comprehensive settlement control in shield tunneling. The optimized parameters are transmitted to the shield machine operator for real-time tuning. During the construction of the shield tunnel, new monitoring data samples are constantly being generated. These will be helpful in future research for further improving the accuracy of the prediction model and enhancing the accuracy of the recommended parameters of the system.

The principle of Bi-LSTM is presented in Section S1 and Fig. S4, the principle of MHSA is presented in Section S2 and Fig. S5, and the principles of RF, PSO, and performance indicators are presented in Sections S3-S5.

### 3 Case study

#### 3.1 Project overview

This section presents an analysis using the Changchun twin-tunnel Metro construction project as a case study and validates the proposed model. The specific section analyzed is the shield tunneling interval between Feiyue Square Station and Eurasia Shopping Mall Station on Section 2 of Line 6 of the

Changchun Metro (ZK16+197.489 to ZK17+575.235), with the shield excavation proceeding from Eurasia Shopping Mall Station toward Feiyue Square Station in the northwest direction, as depicted in Fig. 4(a). Spanning a length of 1,372.44 m, the interval features a minimum curve radius of 550 m and a maximum line gradient of 1.3268%. The overburden above the shield tunnel ranges from 8.7 to 12.3 m. The tunnel excavation occurred in the northwest direction, crossing underneath rain and sewage pipes and gas pipelines and running parallel to the Feiyue Road tunnel. Two EPB shields of model ZTE 6250 from China Railway Heavy Industry Co., Ltd. were used, each with a cutterhead diameter of 6.28 m. As shown in Fig. S6, the cutterhead of the shield is a composite type (4-spoke + panel configuration) with an opening ratio of approximately 38%. The cutterhead is equipped with 4 double-edge toothed cutters at the center, 21 front single-edge toothed cutters, 30 scrapers, 11 edge single-edge alloy disc cutters, and 8 pairs of edge scrapers for bore diameter calibration. The tunnel lining consists of segments with an outer diameter of 6.2 m, a thickness of 0.35 m, and a length of 1.5 m. The center-to-center distance between the twin tunnel axes ranges from 13 to 17 m.

**Changchun Rapid Rail Transit Network (2030 and beyond)**

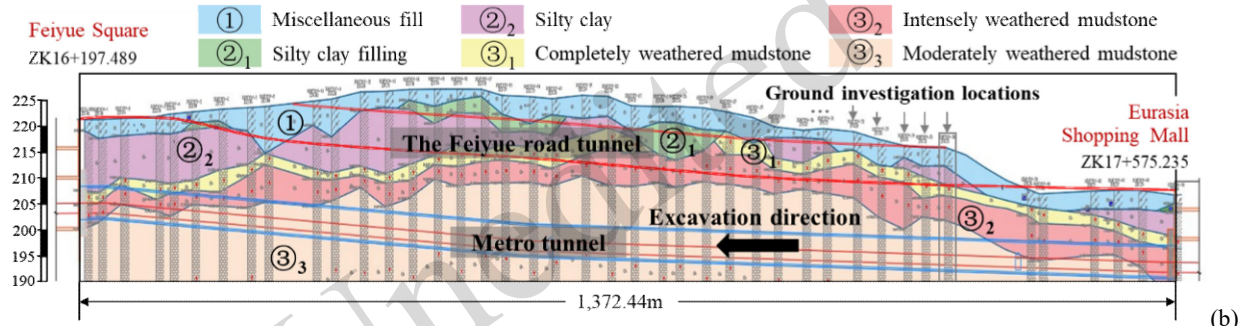
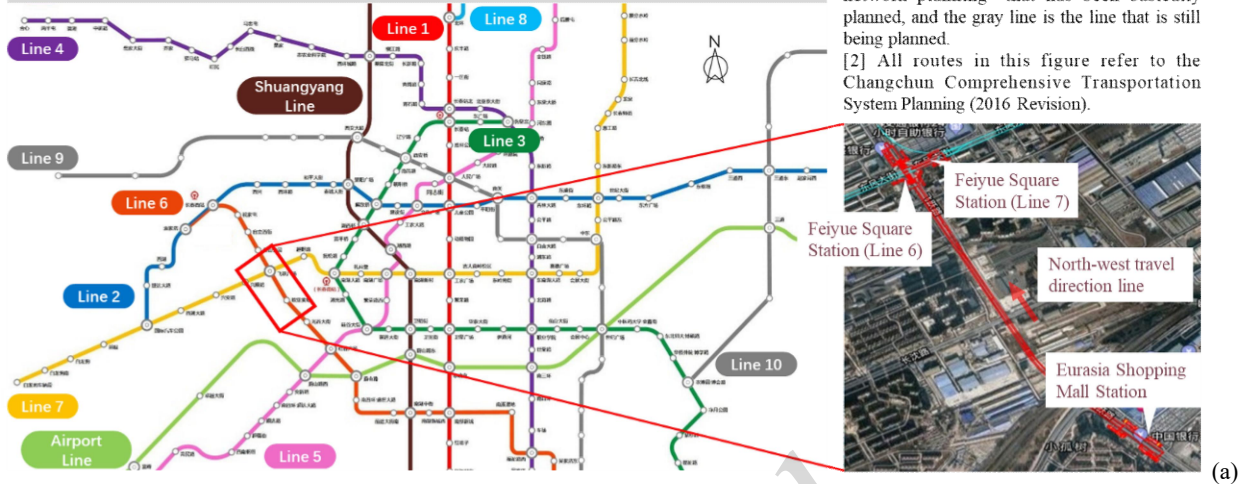


**Fig. 4 Location of construction site: (a) plan view; (b) geological profile**

Fig. 4(b) illustrates the comprehensive geological cross-section of the shield tunneling interval for the northwest travel direction line. The topography of this interval is predominantly flat with an overall gradient from west to east. The stratigraphic description from the uppermost to the lowermost layer is as follows: Miscellaneous fill layer ①, primarily consisting of cohesive soil and construction waste, characterized by a loose structure and inconsistent density, with some areas featuring man-made pavement layers; Silty clay fill layer ②<sub>1</sub>, which is plastic in consistency, mainly composed of arable soil with root systems and a minor content of

crushed stones; Silty clay layer ②<sub>2</sub>, is plastic and slightly soft; Completely weathered mudstone layer ③<sub>1</sub>, intensely weathered mudstone layer ③<sub>2</sub>, moderately weathered mudstone layer ③<sub>3</sub> are susceptible to disintegration upon long-term exposure and readily soften when wet. Table 1 shows the physical and mechanical properties of the geotechnical materials in each layer below the Feiyue Road tunnel. The groundwater table is at a depth of 1.2 to 9.2 m, with an elevation between 195.15 and 229.21 m, predominantly sustained by lateral seepage and throughflow replenishment.

**Table 1 Statistics of the physical and mechanical properties of geotechnical materials**

Geotechnical materials	Density $\rho$ (kg·m <sup>-3</sup> )	Depth (m)	Water content (%)	Void ratio $e$	Liquid limit $W_L$ (%)	Plastic limit $W_P$ (%)	Constrained modulus $E_{oed}$ (MPa)	Cohesion $c$ (kPa)	Angle of internal friction $\varphi$ (°)	Lateral earth pressure coefficient at rest $K_0$
Miscellaneous fill ①	1900	0.2-5.5	22.0	0.84	34.5	19.5	5.5	25	18	0.440

Silty clay fill ②1	-	0.2-9.1	-	-	-	-	-	-	-	-
Silty clay ②2	1960	0.4-16.0	19.9	0.79	28.5	16.5	5.9	29	20	0.425
Completely weathered mudstone ③1	2030	1.5-13.7	18.3	0.72	28.8	18.1	6.2	27	22	0.390
Intensely weathered mudstone ③2	2020	2.0-31.0	17.3	0.68	28.3	17.7	7.4	43	23	0.360
Moderately weathered mudstone ③3	2020	5.4-48.0	15.7	0.62	27.5	17.0	9.9	52	25	0.330

1.  $E_{\text{oed}}$  values determined from oedometer tests over the stress increment range 100-200 kPa (GB/T 50123-2019).

2.  $K_0$  = lateral earth pressure coefficient at rest, determined from laboratory  $K_0$  consolidation tests. The values are lower than those predicted by Jaky's formula for normally consolidated soils, reflecting the residual structural stiffness of the weathered rock mass.

## 3.2 Data preprocessing

### 3.2.1. Data source

A total of 100 sets of parameter values, a sample size comparable to recent shield tunneling machine learning studies (31-137 samples) (Dong et al., 2025, Li et al., 2025, Ye et al., 2023, Zhou et al., 2023b), were sampled from Ring 170 (at ZK17+321.735 on 2022/1/3) to Ring 665 (at ZK16+579.235 on 2022/5/01), with intervals of 5 rings, situated below the Feiyue Road tunnel. The overall structural integrity of the tunnel in this interval reduces the deformation induced by shield tunneling, and the impact of adjacent rings is more significant and cannot be disregarded. Consequently, this presents challenges for conventional machine learning modeling approaches.

### 3.2.2. Fusion of multisource heterogeneous data

Within the framework of Model 1, the influence of a total of 17 variables on the ultimate settlement was examined. The shield tunneling and settlement data are represented in the spatiotemporal domain, where each set of data corresponds to a specific time and location. The geometric and geotechnical parameters are represented in the spatial domain, where each parameter record corresponds to a specific location along the tunneling trajectory. The data fusion process is depicted in Fig. S7.

Geometric and geotechnical parameters were determined from ground investigation reports (GIR). It should be pointed out that the geotechnical parameters given in Table 1 are in the form of mean values. The actual ground investigation locations are

shown in Fig. 4(b), where separate tests were conducted at each corresponding location to obtain the results for determining the parameter values. The root cause of surface settlement during shield tunneling is attributed to the disturbance of the surrounding soil matrix due to construction activities, resulting in a redistribution of soil position and stress. Specifically, the overburden soil above the shield tunnel, being in the direct impact zone of the construction, experienced the most pronounced effects. Therefore, the test results of different soil layers at each sampling position were interpolated linearly and mapped onto each shield ring position. The physical and mechanical parameters were weighted according to the thickness of different soil layers and averaged, as shown in Fig. S7.

The shield operation parameters were monitored by the system in real time, removing data from the shutdown phase using parametric multiplication methods (Chen et al., 2023, Zhang et al., 2022). Given the noncontinuous nature of the construction process, specific data selection was refined to minimize the effects of noise and outliers. The excavation chamber behind the cutterhead is typically maintained at a level between half-full and full, and  $P_S$  was determined by averaging the pressure at the excavation face. Parameters such as  $S_A$  and  $R_C$  were determined by the average of the corresponding ring positions.

To synchronize the surface settlement data with shield operation parameters, measurements were taken along the longitudinal axis of the tunnel at the same intervals of 7.5 m for 12 hours, with an increased monitoring frequency of 3 hours near the

shield excavation position. Surface settlements 10 days after completion of ring boring were used to assess  $S_s$ . The preshield arrival surface settlements  $S_{PS0}$  and  $S_{PS7.5}$  are the surface settlements at a location when the shield arrives at that location and when the shield is 7.5 m before arriving at that location.

### 3.2.3. Data division and standardization

The first 80% of the datasets were used for model development, and the remaining 20% of the data constituted the test dataset, which was used to validate the accuracy and validity of the predictive model. Table S1 delineates the input and output parameters within Model 1 along with their respective value ranges.

The parameters of the samples encompassed disparate units of measurement and exhibited substantially different value ranges. Direct model training without prior adjustment could result in a degradation of accuracy. To bolster the precision of the model's predictions and to hasten the convergence of algorithms, the training data underwent min-max normalization, transforming it to the interval [0,1].

## 4 Results and discussion

### 4.1 Settlement prediction and comparative analysis

In the conceptualization of Model 1, as a successor to traditional empirical or numerical models, prediction accuracy was prioritized. While increasing hidden layers can capture complex patterns, 1-3 layers balance complexity and performance. (Shen et al., 2021). As shown in Fig. S8, a two-layer Bi-LSTM architecture was adopted. The first Bi-LSTM layer (L1) processed sequential features bidirectionally, capturing short-term dependencies. A self-attention layer followed L1,

projecting its output into  $h$  subspaces (heads) to compute contextual weights. A dropout layer regularized the attention output to prevent overfitting. The second Bi-LSTM layer (L2) integrated attention-weighted features, enhancing long-term dependency capture through bidirectional recurrence. The optimizer was configured to Adaptive Moment Estimation (Adam), with the training process set to complete after 500 epochs. To mitigate instability during the training process, the learning rate was modulated using a piecewise schedule strategy, commencing with an initial learning rate ( $lr$ ) = 0.001 (dimensionless), with the learning rate reduced by a drop factor of 0.15 after 400 epochs. The grid search method (GSM) was used to determine various hyperparameters in the model, including the stride  $seq$  [1:1:5] (searched over 1 to 5 in increments of 1, the following text is similar), the number of hidden units  $hs1$  and  $hs2$  [10:10:500] in the Bi-LSTM layer, the dropout rate  $dp$  [0.1:0.05:0.6] in the Dropout layer, the number of heads [2:1:10] and the number of key channels [1:1:10 times the number of heads] in the Self Attention layer. The 5-fold time-series cross-validation (5-TCV) method was utilized to determine the optimal architecture of the proposed models. The comparative analysis involved four extensively utilized models: SVR (Sun, 2022), RF (Zhang et al., 2020c), Transformer and Bi-LSTM (Zhou et al., 2023b). For these comparative models, the quantity of input and output parameter units, as well as the number of training epochs, were consistent with those of the MHSA-Bi-LSTM model. The remaining hyperparameters were optimally determined using the GSM. The aforementioned modeling procedures were executed in MATLAB and Python 3.10, and the specific hyperparameter settings determined for the models are detailed in Table 2.

**Table 2 Values of optimum hyperparameters in ML models**

Model	Optimum hyperparameters
MHSA-Bi-LSTM	$seq = 2$ , Number of key channels = 20, Number of heads = 4, $hs1 = 120$ , $hs2 = 80$ , $dp = 0.5$ , $lr = 0.001$ , Batch size = 20
Bi-LSTM	$seq = 2$ , $hs1 = 200$ , $hs2 = 160$ , $dp = 0.3$ , $lr = 0.001$ , Batch size = 20
Transformer	$seq = 1$ , Embed dim=31, Number of heads = 1, Feedforward network dim = 16, $dp = 0.28$ , $lr = 0.001$
RF*	Number of decision trees ( $tr$ ) = 136, The minimum number of leaf node samples ( $lf$ ) = 5
SVR*	$C$ _ Penalty parameter = 1.414, $g$ _ Smoothing parameter of kernel function (RFB) = 0.707

Models marked with '\*' are unable to capture  $S_s$  spatial features due to structural limitations.

The models were trained based on their respective structural parameters, and the test set was employed to conduct predictive analyses for each model. The predicted results and relative errors are

depicted in Fig. 5. All samples were predicted, and the predicted results and evaluation indicators of each model were obtained, as shown in Fig. S9.

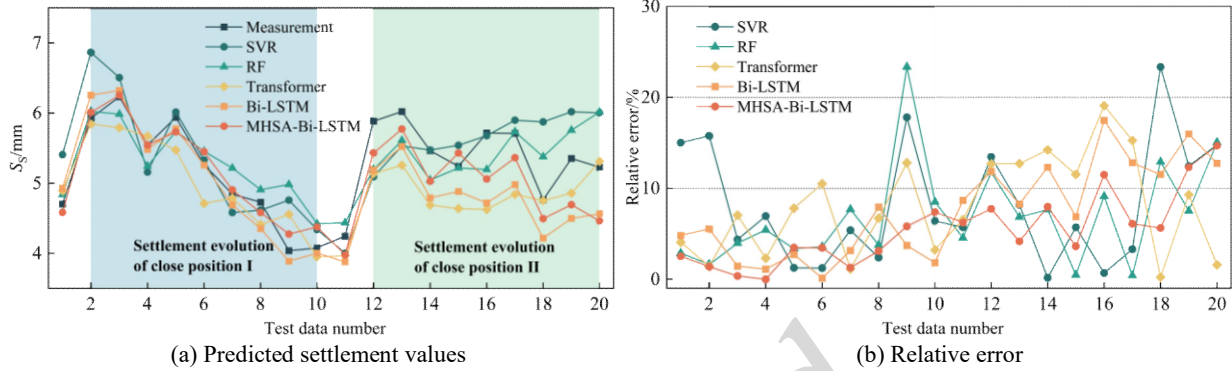


Fig. 5 Predicted results of the test set

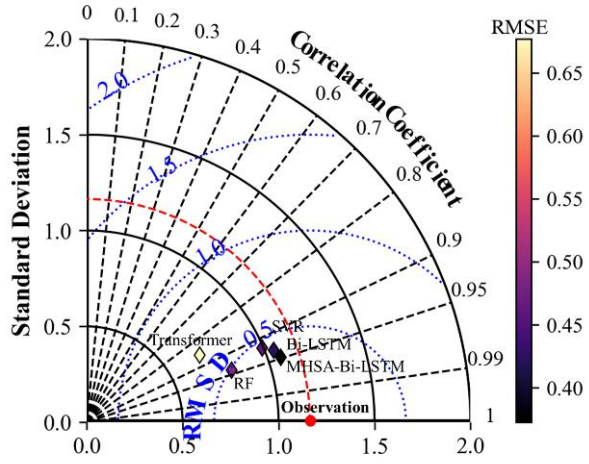
Fig. 5 illustrates that over 90% of the relative errors for the test set predictions from the five models are contained within 20%. This signifies the capability of ML techniques to discern the intrinsic correlations between shield operation parameters, geotechnical parameters, and shield settlement, indicating that the selection of input parameters is reasonably justified. Additionally, the input of  $S_{PS}$  gives the model a good predictive performance. In contrast to the average relative errors of 8.21% for the SVR model, 7.02% for the RF model, 8.00% for the transformer model, and 7.54% for the Bi-LSTM model, the MHSA-Bi-LSTM model has achieved a reduction to 5.22%, with the prediction errors for 85% of the samples being confined within 10%. However, in the other models, the samples satisfying this criterion have not surpassed 80%. As depicted in Fig. 5(a), the Transformer, Bi-LSTM and MHSA-Bi-LSTM models have almost perfectly captured the spatial correlation across two distinct intervals. The latter effectively focused on important features, resulting in predicted results closer to the actual measurements. Overall, the MHSA-Bi-LSTM model exhibited superior performance in predictive accuracy and error stability.

Fig. S9 shows the predictive performance of each model. The closer the scatter points are to the diagonal, the more accurate the model's predictions. The SVR model, which constructs a hyperplane or an approximation function in high-dimensional feature space for regression, tends to determine a cautious

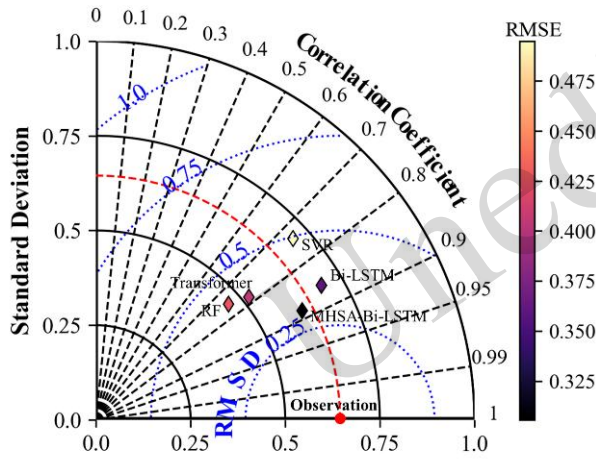
predicted value to samples to account for uncertainties, thus trading off some level of precision. The RF model is not able to capture spatial relationships due to structural limitations and showed good performance with the training sets but not the best performance with the test set. Although both the Transformer and Bi-LSTM models have the ability to capture long-term dependencies, the former performs unsatisfactorily on the training and validation sets, while the latter has a better overall performance. The MHSA-Bi-LSTM model outperformed all the other models in the test set for  $S_s$  prediction, with MAE, RMSE, and  $R^2$  values of 0.283, 0.352, and 0.78, respectively. This superior performance is credited to its enhanced memory retention and attention mechanisms, indicating that the model possesses optimal predictive accuracy for forecasting the surface settlement during shield tunneling operations.

Fig. 6 shows the standard Taylor diagram (Taylor, 2001) of the predicted results of all the models, where the black dashed lines represent the Pearson correlation coefficient ( $r$ ), the blue dotted lines represent the root mean squared difference (RMSD, which is conceptually related but not identical to RMSE), the solid lines represent the standard deviation, and the red dot represents the observation point. The closer each index value is to the observation point, the more accurate the prediction results are. It is obvious that the MHSA-Bi-LSTM model is closer to the observation point compared to others, which means it is more

competitive than the other models.



(a) Training & validation sets



(b) Test set

Fig. 6 Standard Taylor graph of models

### 4.2 Sensitivity analysis of parameters affecting $S_s$

Sensitivity analysis methodologies are instrumental in determining the importance of input variables to models or systems and are frequently applied to evaluate the degree of output variation attributable to parameter uncertainties, significantly contributing to the identification of parameter priorities and dimension reduction (Liu and Ding, 2020). Despite the computational simplicity and speed of local sensitivity analysis (LSA), its heavy reliance on nominal value positions and lack of insight into the true value locations make it inappropriate for shield tunneling systems characterized by high levels of parameter uncertainty (Cheng et al., 2016). Global sensitivity analysis

(GSA), on the other hand, captures the influence of the entire input parameter space on the model outcomes, independent of the need to predefine optimal positions and effectively circumvent the constraints of LSA.

This research employs the Sobol method (Liu and Ding, 2020, Sobol, 2001) within GSA to examine the extent to which various parameters affect  $S_s$ . Suppose the proxy model is  $Y = f(\mathbf{X})$ , the unconditional variance  $V(Y)$  can be decomposed into partial variances accordingly, where  $V_i$  and  $V_{ij}$  represent the variances of  $f_i$  and  $f_{ij}$ , respectively:

$$V(Y) = \int_{\Omega} f^2(\mathbf{X})d\mathbf{X} - f_0^2 \quad (1)$$

$$= \sum_{i=1}^t V_i + \sum_{i=1}^{t-1} \sum_{j=i+1}^t V_{ij} + \dots + V_{1,\dots,t}$$

Using these variations, first-order, second-order, and total Sobol sensitivity indicators can be defined according to the total variance:

$$MSI = S_i = \frac{V_i}{V(Y)} = \frac{V_{x_i} [E_{X \sim x_i} (Y | x_i)]}{V(Y)} \quad (2)$$

$$S_{ij} = \frac{V_{ij}}{V(Y)} = \frac{V_{x_i, x_j} [E_{X \sim x_i, x_j} (Y | X \sim x_i, x_j)]}{V(Y)} \quad (3)$$

$$TSI = ST_i = 1 - \frac{V_{\sim i}}{V(Y)} = \frac{E_{X \sim x_i, x_j} [V_{x_i, x_j} (Y | X \sim x_i)]}{V(Y)} \quad (4)$$

The main sensitivity index (MSI) or first-order index  $S_i$  indicates the degree of disturbance to the output when a single input  $x_i$  value fluctuates. The second-order index  $S_{ij}$  or second-order interaction effect index of  $x_i$  and  $x_j$  characterizes the degree of disturbance to the output caused by the interaction between the two inputs.  $V_{\sim i}$  is the bias variance corresponding to the remaining indicators except  $x_i$ . The total effect  $ST_i$ , namely, the total sensitivity index (TSI), characterizes the total degree of disturbance of the output by all the effects caused by the input indicator  $x_i$  when the value of the input indicator  $x_i$  fluctuates and can be interpreted as the sum of the sensitivity indices of each order for that input

indicator.

Utilizing the MHSA-Bi-LSTM model constructed as a surrogate model and based on the parameter variable range, Latin hypercube sampling

(LHS) (Dige and Diwekar, 2018) is performed, followed by correlation computations to determine the MSI and TSI for each parameter across different sample sizes, as illustrated in Fig. 7.

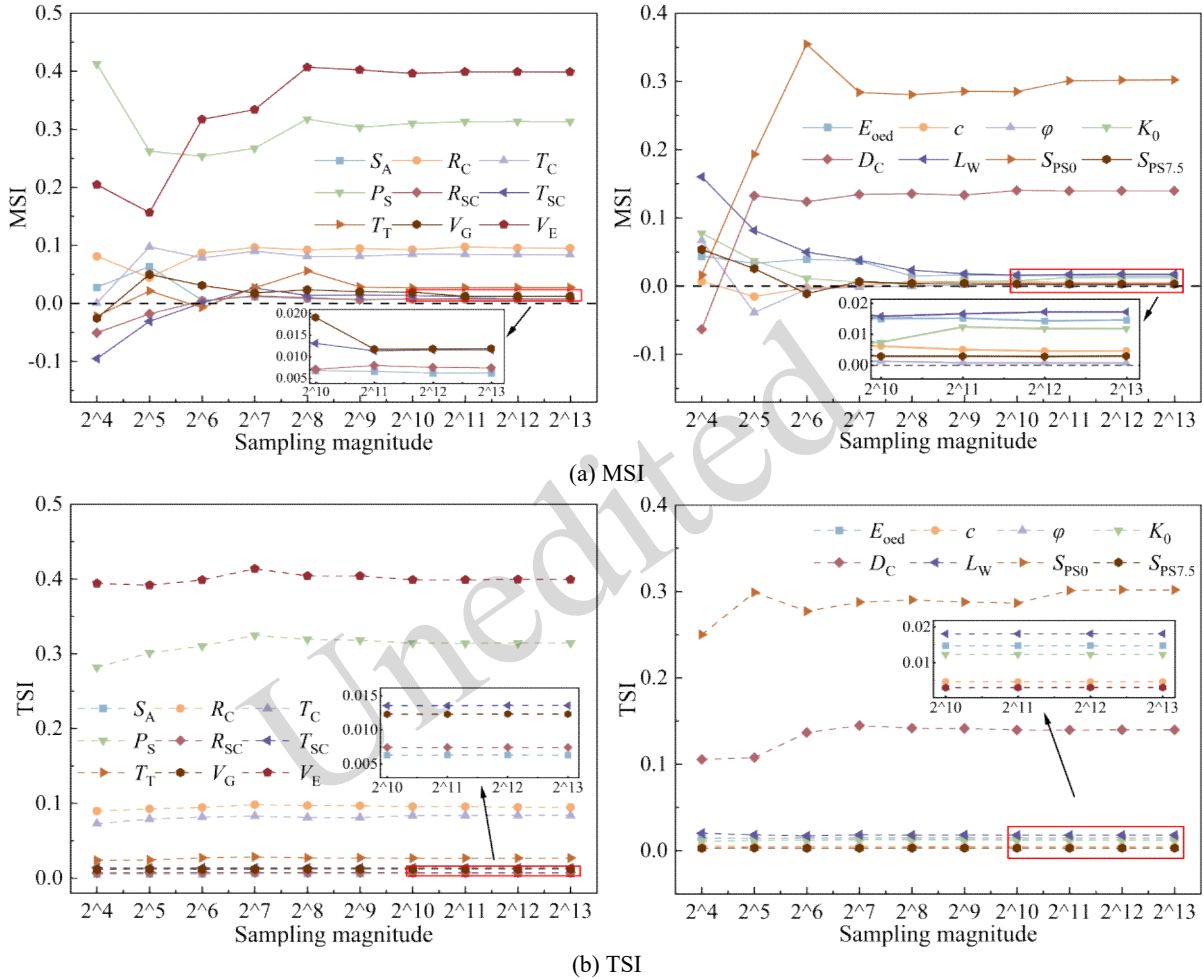


Fig. 7 Parameter sensitivity

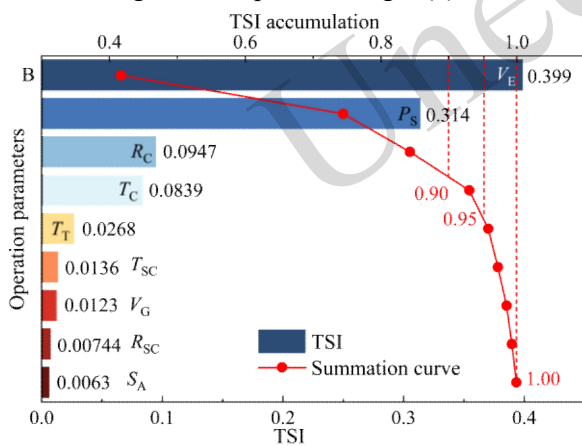
Overall, when the sampling magnitude exceeds  $2^{11}$ , the ranking of sensitive input parameters by MSI and TSI is stable. The primary and total effects of the parameters exhibit no marked variations in their order, suggesting that the interactive effects among inputs have a limited impact on the surface settlement. As evident from the stable sensitivity index values in the right panels of Fig. 7, the effects of  $S_{PS}$  and uncontrollable geometric and geotechnical conditions have a certain degree of influence on  $S_s$ , with their aggregate TSI values summing to approximately 0.50. In the calculation results, the MSI and TSI of  $V_E$ ,  $P_S$ ,  $R_C$ , and  $T_C$  are relatively large, indicating that these parameters have a great influence on  $S_s$ .

Consequently, these parameter indicators should be prioritized during the optimization and control processes for  $S_s$ .

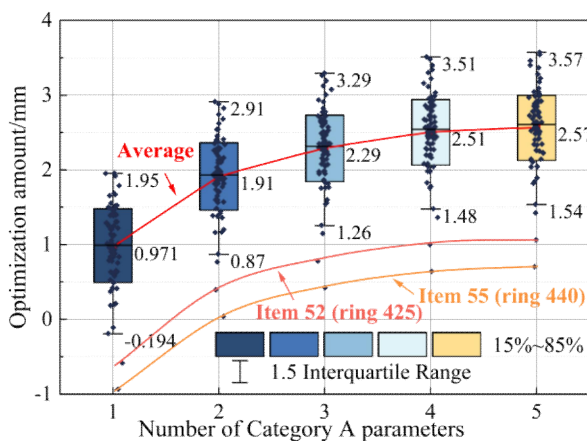
### 4.3 Operation parameter adjustment based on the integration mechanism

The workflow mechanism in Fig. 3 indicates that the selection of Category A parameters is pivotal in determining the extent of optimization, whereas Category B and C parameters delineate the interdependencies among the operation parameters. To balance optimization effectiveness with practical application scenarios, this study assessed the  $S_s$  optimization capabilities with varying quantities of

Category A parameters. At most, the top 5 most sensitive parameters were selected for optimal search as Category A parameters, since at this point, as shown in Fig. 8(a), the cumulative TSI results are over 90% and have absolute influence. The PSO method was employed as an optimization approach for Category A parameters. The  $S_s$  outcomes forecasted by the meta-model were adopted as the fitness function for PSO. The position vector within the PSO method was substituted with the Category A parameters that were targeted for optimization. The goal of the algorithm was to determine a suitable position vector, that is, the shield operation parameters, which resulted in minimization of the fitness value. Within the PSO methodology, the iteration count was fixed at 100, the swarm size at 50, the acceleration coefficients  $C1$  and  $C2=1.5$ , and the inertia weight at  $w=0.8$ . The range of parameter values was determined by the extremities of the monitored data. The detailed procedures are outlined in Section S4, and the  $S_s$  optimization amount derived from training sets is depicted in Fig. 8(b).



(a) TSI accumulation of operation parameter



(b) Optimization amount

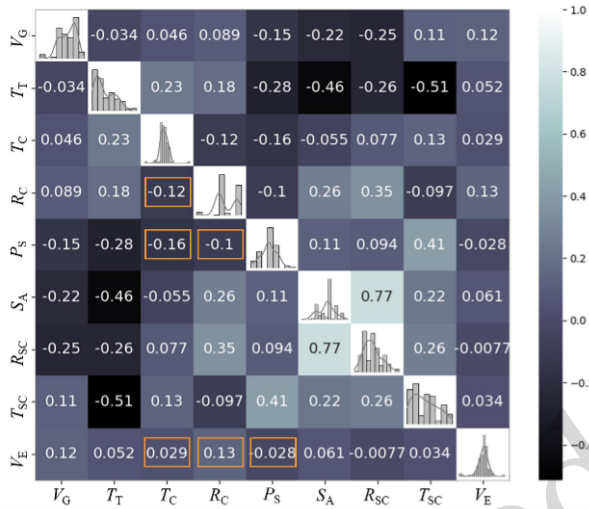
Fig. 8  $S_s$  optimization results for training sets under different numbers of Category A parameters

Fig. 8(b) shows that most of the optimized results are markedly lower than the initial estimates, with minimal optimization effects observed for item 52 (ring 425) and item 55 (ring 440). This suggests that the geometric and geotechnical parameters are predominantly responsible for  $S_s$  at these points, while the influence of the shield operation parameters is comparatively minor. However, the optimization plateaus when the number of Category A parameters exceeds four. Due to the waning global sensitivity of the additional parameters and the persistent impact of geometric and geotechnical parameters in the meta-model, the optimization speed of the predicted  $S_s$  value slows down and gradually converges.

In the 4-parameter optimization, the optimized recommended values of  $A1(V_E)$ ,  $A2(P_S)$ ,  $A3(R_C)$ , and  $A4(T_C)$  for each ring position are located at the extreme values of 63.09 m<sup>3</sup> (Min), 1.5 bar (Max), 1.5 rpm (Min), and 1.4 MN·m (Min), respectively. This is not difficult to explain and indicates that within the constrained range, there is a strong monotonic relationship between these input parameters and  $S_s$ . Specifically, a decrease in  $V_E$ ,  $R_C$ , and  $T_C$  results in diminished disturbance to the excavation face and the soil surrounding the shield, consequently yielding relatively reduced surface settlement. Conversely, an elevation in  $P_S$  creates a more densely compacted zone ahead of the shield, where soil particles undergo compaction, enhancing the soil density and, by extension, reducing its compressibility. This reduction in compressibility subsequently mitigates ground surface settlement. These observations further substantiate the alignment of the mapping relationship with reality.

As shown in Fig. 9, there are varying degrees of correlation among the operation parameters, where Pearson correlation coefficients (PCCs) greater than 0.2 indicate a certain degree of correlation. Optimizing all the parameters completely destroys this intrinsic relationship, leading to physically unrealistic combinations. The cells highlighted with orange borders denote the six pairwise PCCs among the four Category A parameters ( $V_E$ ,  $P_S$ ,  $R_C$ , and  $T_C$ ). All highlighted values exhibit low absolute PCCs ( $|PCC| \leq 0.2$ ), confirming that these four parameters

are largely mutually independent. This weak intercorrelation supports the selection of four Category A parameters for direct optimization, as adjusting them simultaneously does not severely disrupt the intrinsic relationships within the operation parameter system.



**Fig. 9 Correlation matrix of operation parameters heatmap**

On the main diagonal of Fig. 9, frequency distribution histograms are presented for each individual parameter in place of the trivial self-correlation value of 1.0. For instance, the detailed fitted distributions of  $T_C$  and  $V_E$  are presented in Fig. S12 (Section 4.4), where their implications for the interpretation of optimization results are discussed.

Many interactions between parameters have been discovered, such as  $V_E$  being intricately linked to stratum parameters,  $S_A$ ,  $R_{SC}$ , and  $T_{SC}$ . (Huang et al., 2022). Similarly,  $P_S$  is closely associated with  $T_T$ ,  $S_A$ ,  $T_C$ ,  $R_C$ ,  $R_{SC}$ ,  $T_{SC}$ , etc. (Lin et al., 2021). To attain more accurate recommendations while conforming to practical conditions on site, a hierarchical inversion method is introduced. As shown in Fig. 3, the study primarily employs inverse Model 2 to backtrack Category B for uncontrollable parameters (B1:  $T_T$ , B2:  $T_{SC}$ , B3:  $V_G$ ), using geometric and geotechnical parameters, updated Category A parameters, and settlements as inputs. Subsequently, Category C for artificially regulated parameters (C1:  $R_{SC}$ , C2:  $S_A$ ) is backtracked in Model 3 using all the aforementioned parameters (updated). The variable details for Models 2 and 3 are presented in Table S2.

In the data distribution, it was found that some of the operation parameters that need to be inverted have limited monitoring accuracy. The LSTM, transformer, etc., models are based on back-propagation algorithms, which may affect the state update in subsequent sequence steps and can lead to large deviations in the predicted results (Rashid et al., 2018, Tsai and Cho, 2021). Ensemble learning algorithms, such as RF, exhibit good stability and robustness when data anomalies occur (Hia et al., 2023) and are used for inversion prediction of Category B and C parameters. The SVR algorithm, which also exhibits excellent robustness (Hou et al., 2020), is used for comparison. GSM and 5-fold cross-validation are used as a hyperparameter (as shown in the brackets of the annotations in Figs. S10 and S11) optimization method, and the training and inversion results for Category B and C parameters are shown in Figs. S10 and S11, respectively.

Figs. S10 and S11 show the predicted and inversion results for shield operation parameters using Models 2 and 3. The prediction performance of the five parameters is generally good. The distribution of some Category B parameters is more concentrated due to the limitation of monitoring accuracy, which will inevitably be affected in the inversion prediction. The adjustment steps set by the staff for the parameters of Category C parameters are large, and the positions of many points are fixed, which leads to some deviations in the predicted results. The SVR model is more susceptible to monitoring accuracy, resulting in increased errors, while the RF model has superior predictive performance, with average reductions of 27.46% and 27.03% in MAE and RMSE in the test set. It is obvious that the MAE and RMSE values of the Category B2 and C2 parameters are much higher than those of the remaining three parameters because the order of magnitude and the range of values of  $T_{SC}$  and  $S_A$  are larger than those of the other shield operation parameters.

In practical engineering applications, the primary concern is reasonable control, followed by avoiding frequent adjustments, which indicates that the inversion of operating parameters requires higher precision. Fig. S10 shows that the range of variation in the controllable parameter inversion results of the SVR model is very small, which is abnormal in practice. For example, take the  $R_{SC}$ - $S_A$  relationship in

Fig. 9, which exhibits the most significant linear relationship (PCC  $r = 0.77$ , with  $|r|$  closest to 1.0 among all parameter pairs, indicating the strongest linear correlation in the matrix), as an example and perform a Fisher's Z test. As shown in Fig. 10, when using the RF and SVR models, the z values for the correlation coefficients between the inversion results and the initial values are -1.427 and 1.029 ( $<1.96$ ), respectively, with p values of 0.153 and 0.303 ( $>0.05$ ), indicating that the differences in correlation coefficients are not significant. The slope difference of the RF model is 0.667, the t-statistic is 1.723 ( $<1.96$ ), and the p value is 0.087 ( $>0.05$ ), indicating no significant difference in the linear relationship between the data before and after inversion. However, the slope difference of the SVR model is -2.676, the t-statistic is -9.120 ( $<-1.96$ ), and the p value is extremely small ( $2.22e-16$ ), indicating a highly significant difference. In contrast, the RF model performs exceptionally well, which is more appropriate for consideration.

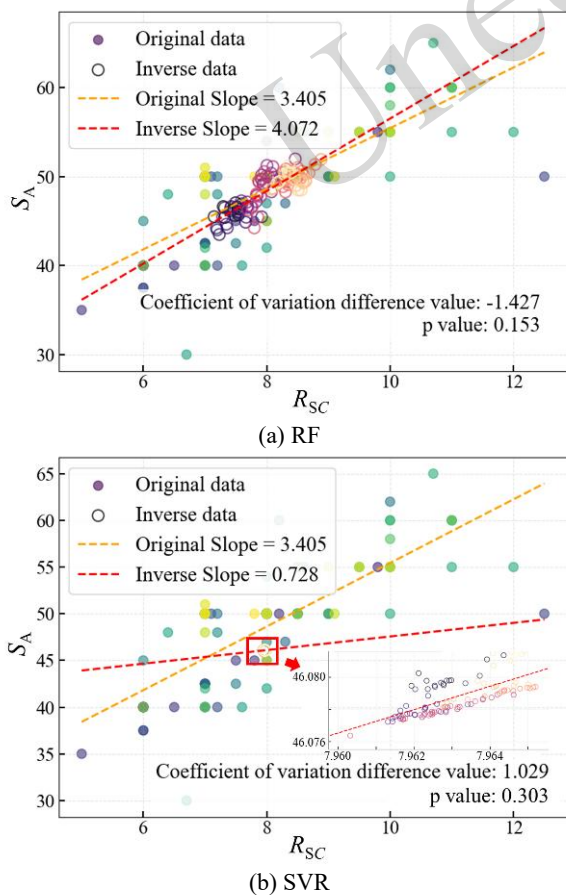


Fig. 10 The scattered distribution of  $R_{SC}$ - $S_A$

#### 4.4 Mechanism verification and qualification

To evaluate the reliability and feasibility of the research framework for shield parameter self-adaptation, the updated parameters, following the completion of all optimization procedures, are introduced in place of the initial operation parameters into the settlement prediction meta-model. Given that the precision of Model 1 has been confirmed in prior sections, it is justifiable to regard the new predictive outcomes as reliable. By adjusting the parameters of the test set using the proposed method, the optimized  $S_s$  obtained are shown in Fig. 11.

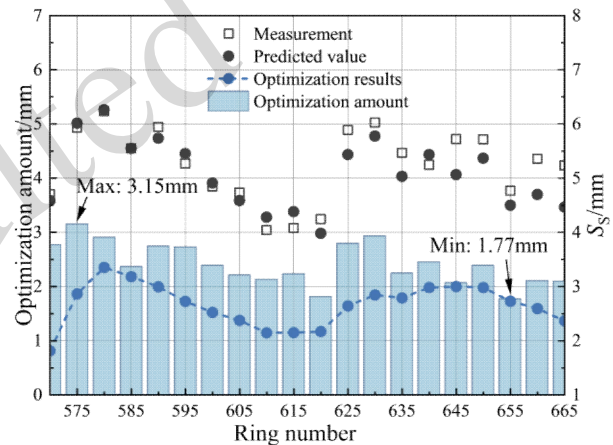


Fig. 11 The results of the adaptive adjustment strategy in the test set

The results in Fig. 11 show that the optimized surface settlements  $S_s$  are reduced for all ring positions in the test set. The predicted  $S_s$  of the adaptive adjustment strategy were reduced by an average of 2.41 mm (47.55%). A comparison with the actual measurements shows that, with a few exceptions, the surface settlements were significantly reduced by an average of 2.59 mm (49.28%). In conclusion, the integration mechanism of optimization and inversion shows a strong ability to control settlement.

In subsequent shield construction, the adaptive adjustment strategy proposed in this study (applied to rings 815-910) contrasts sharply with the full optimization strategy proposed by Hou et al. (2020) (applied to rings 715-810), mainly using the minimum  $S_s$  as the objective function and directly searching all shield operation parameters through an

optimization algorithm. As shown in Fig. 12, the full optimization strategy performs global optimization of all the operation parameters without distinguishing between the controllability and sensitivity differences of parameters, leading to adjustments of uncontrollable parameters (such as  $T_T$ ,  $V_G$ ,  $T_{SC}$ ) deviating from actual engineering constraints. In contrast, the adaptive mechanism considers the synergistic values of all the shield operation parameters under all geometric and ground conditions, with adjustments to uncontrollable parameters better aligning with actual engineering constraints. Notably, there is a certain discrepancy

between the recommended results (minimum values) for  $T_C$  and  $V_E$  and the actual results. This is because the minimum values for these two operation parameters are prominent in the initial data distribution (see Fig. S12 from Fig. 9) and may be generated under special ground conditions. However, the test section may lack the necessary conditions to achieve extreme values, and the adaptive adjustment strategy's parameter variations in Category B and C parameters further constrain the actual results for  $T_C$  and  $V_E$ . Thus, while unable to reach the theoretical minimum, they remain very close to it.

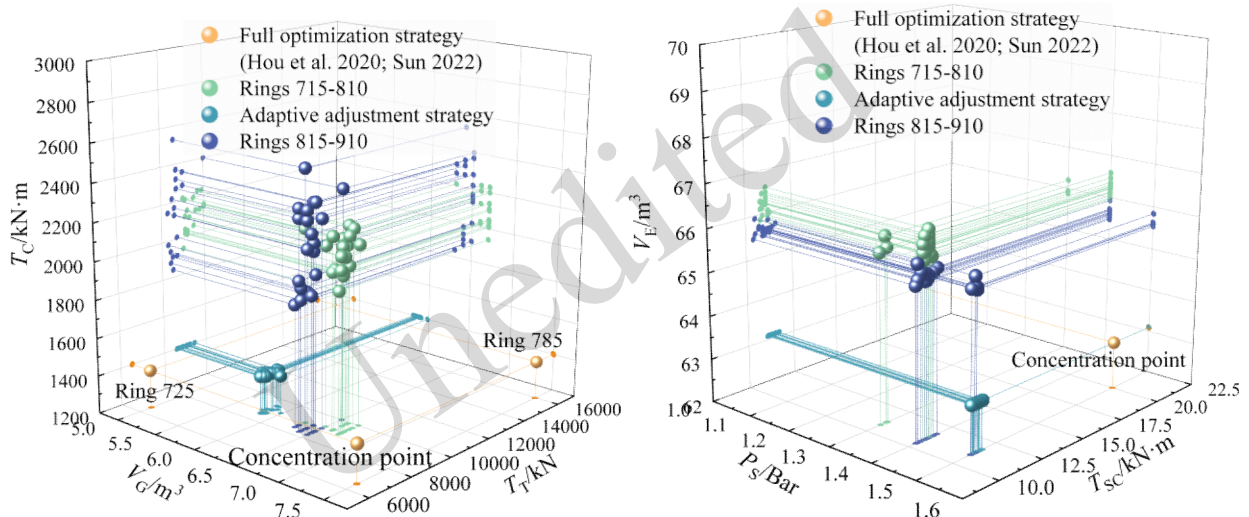


Fig. 12 Distributions of the uncontrollable parameters of rings 715-910 in theory and practice

Based on the actual monitored data, the results of the uncontrollable parameters in the full optimization strategy exhibit an average deviation of  $\pm 34.27\%$  from the theoretical target values. The coupling effects with the ground conditions are ignored, leading to an imbalance in the matching of parameters such as  $P_S$  and  $T_T$ . In contrast, the average fluctuation in the results of uncontrollable parameters in the adaptive mechanism is only  $\pm 13.95\%$ , and their trend of change exhibits significant synergy with the optimization direction of controllable parameters: when  $P_S$  is optimized to 1.4-1.5 bar,  $T_T$  automatically matches 8-10 MN (an improvement of 37.9% over 6.5 MN by the Hou method), which aligns with the coupling effects in the geotechnical parameters and conforms to the mechanical force transmission principles of an EPB shield.

Fig. 13 shows the initial predicted surface

settlements and measured  $S_S$  values in the two execution strategies of rings 715-910. In the full optimization strategy, the predicted settlement is smaller, but the actual average increase in  $S_S$  is 1.47 mm. This is primarily because the interaction relationship constraints cause changes in the uncontrollable parameters, thereby leading to significant control errors. In contrast, the adaptive adjustment strategy achieves smaller predicted settlement errors through collaborative parameter values, with an average increase in  $S_S$  of 0.32 mm. The average values of the two strategies were 4.72 mm and 3.81 mm, respectively, representing improvements of 23.25% and 38.05% compared to the baseline average  $S_S$  of 6.15 mm (rings 170-665 without optimization). The latter strategy demonstrated significantly superior precontrol effects on surface settlement caused by shield tunneling

compared to the former strategy.

The study used a novel automation to reduce the effects of interactions between shield operation parameters and to precontrol  $S_s$ . We believe that the methodology proposed in this study will provide a versatile scientific solution for the control of surface settlement caused by shield tunneling and the refinement of operational parameters. The  $S_s$  forecast model's training dataset was primarily based on weathered mudstone and silty clay profiles. The miscellaneous fill layer encountered at the subsequent positions of the tunnel exhibits mechanical properties that slightly deviate from the training distribution. Consequently, while the model captures the general behavioral trends in such zones, the quantitative accuracy may be lower compared to well-represented layers. In future studies, we aim to expand the training dataset to include a wider variety of anthropogenic fill layers and incorporate micromechanical indicators to enhance the model's robustness when encountering ground conditions whose mechanical properties fall outside the range represented in the training dataset.

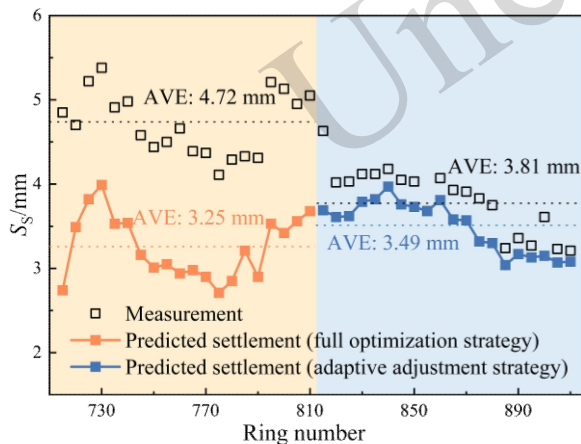


Fig. 13  $S_s$  results for rings 715-910

## 5 Conclusions

Considering the controllability of parameters and their interactive synergies in practical shield engineering contexts, this research introduces an adjusting approach for shield operation parameters that integrates optimization and inversion. Initially, a meta-model (MHSA-Bi-LSTM) considering preshield arrival surface settlement is established for real-time prediction of  $S_s$ . The parameters that are dominant regarding predicting  $S_s$  and the parameters

that  $S_s$  is most sensitive to are searched using the PSO method, while the parameters that  $S_s$  is less sensitive to are predicted through inverse models, constructing a hybrid optimization mechanism by combining the two. Implementing this method in practical construction facilitates the self-adaptation of the EPB shield operation and preemptive control over shield tunneling-induced surface settlement. The primary conclusions are summarized as follows:

(1) During the development of Model 1 utilizing diverse methodologies, the settlement predictions made by the MHSA-Bi-LSTM model demonstrated a high degree of concordance with the empirically measured settlements, with an MAE of 0.283, RMSE of 0.352, and  $R^2$  of 0.78. The superior predictive performance of the MHSA-Bi-LSTM model compared to the Bi-LSTM, Transformer, RF, and SVR models (Fig. S9) is credited to its enhanced memory retention and multihead self-attention mechanisms, which effectively capture spatiotemporal dependencies in shield tunneling data.

(2) GSA utilizing the Sobol method has demonstrated that within the nine shield operation parameters under consideration, a significant correlation exists between the surface settlement and  $V_E$  and  $P_s$ , as well as the cutterhead parameters including  $R_C$  and  $T_C$ , which is consistent with the theoretical study. Optimization of Category A shield operation parameters identified that within a certain range, a decrease in  $V_E$ ,  $R_C$ , and  $T_C$ , along with an increase in  $P_s$ , can have a reducing effect on the surface settlement induced.

(3) Addressing scenarios with limited monitoring accuracy, the RF model was adapted to construct inverse Models 2 and 3 predictions for Category B and C shield operation parameters. The results obtained using the RF model are more accurate than the results obtained using the SVR model, and the MAE and RMSE values of the test set were reduced by 27.46% and 27.03%, respectively, on average.

(4) During the validation of the effectiveness of the adaptive method, the predicted values of  $S_s$  for the test set of the method were reduced to a certain extent, with an average reduction of 2.41 mm (47.55%) and an average reduction of 2.59 mm (49.28%) compared to the measured values.

(5) The adaptive adjustment strategy

demonstrated significant advantages in regulating the uncontrollable parameters compared with Hou et al. (2020)'s full optimization strategy. The full optimization strategy caused an average deviation of  $\pm 34.27\%$  in uncontrollable parameters from theoretical targets, ignoring the coupling effects with the ground conditions and leading to imbalances in parameter matching. In contrast, the adaptive strategy mechanism restricted the average fluctuation of the uncontrollable parameters to  $\pm 13.95\%$ , and the trend of parameter changes showed significant synergy with the optimization direction of controllable parameters.

(6) On-site verification showed that in the full optimization strategy, changes in uncontrollable parameters under interaction constraints led to significant control error. In contrast, the adaptive strategy mechanism achieved smaller prediction errors through collaborative parameter values, with an average increase of only 0.32 mm in  $S_s$ . Compared with the baseline average  $S_s$  of 6.15 mm (rings 170–665 without optimization), the average  $S_s$  values of the full optimization strategy and the adaptive adjustment strategy are 4.72 mm and 3.81 mm, representing improvements of 23.25% and 38.05%, respectively. This indicated that the adaptive mechanism has significantly superior precontrol effects on shield tunneling-induced surface settlement.

It should be emphasized that the factors examined in the study are among the most frequently encountered and are universally adaptable. However, the study did not touch upon specific factors required in special ground conditions (e.g., the need to consider the location and size of karst caves or the implementation of special support and reinforcement measures in soft ground), which are aspects that need to be investigated in the future.

### Acknowledgments

This work was supported by China Railway 22nd Bureau Group Track Engineering Co., Ltd.

### Author contributions

Dongsheng Wei: Writing-original draft, Validation, Software, Methodology, Investigation, Conceptualization. Haibin Wei: Supervision. Zipeng Ma: Writing-review & editing, Supervision. Heting Wei: Writing-review & editing, Supervision. Lijie Sun: Supervision. Xiaokun Yu: Supervision.

### Conflict of interest

The authors declare that they have no known competing financial interests or personal relationships that could have appeared to influence the work reported in this paper.

### Data availability

The data that support the findings of this study are available from the corresponding author upon reasonable request.

### References

- Al Mehedi MA, Amur A, Metcalf J, et al., 2023. Predicting the performance of green stormwater infrastructure using multivariate long short-term memory (LSTM) neural network. *Journal of Hydrology*, 625:130076. <https://doi.org/10.1016/j.jhydrol.2023.130076>
- Bao WJ, Su WZ, Zhao X, et al., 2025. A study on short-term vegetable price prediction based on the CNN-LSTM-Attention model. *Discover Food*, 5(1). <https://doi.org/10.1007/s44187-025-00426-2>
- Chen HY, Li XY, Feng ZB, et al., 2023. Shield attitude prediction based on Bayesian-LGBM machine learning. *Information Sciences*, 632:105-129. <https://doi.org/10.1016/j.ins.2023.03.004>
- Chen RP, Zou N, Wu HN, et al., 2022. Review of prediction and control for surface settlement caused by shield tunneling based on machine learning. *Journal of Huazhong University of Science and Technology (Natural Science Edition)*, 50(8):56-65. <https://doi.org/10.13245/j.hust.220806>
- Cheng JCP, Lu QQ and Deng YC, 2016. Analytical review and evaluation of civil information modeling. *Automation in Construction*, 67:31-47. <https://doi.org/10.1016/j.autcon.2016.02.006>
- Cheng XS, Zhang SL, Zhou XH, et al., 2022. Parameter analysis of excavation face stability of shield tunnel under high water pressure seepage. *Physics and Chemistry of the Earth*, 128. <https://doi.org/10.1016/j.pce.2022.103218>
- Deng XH and Wang BL, 2013. Analysis of Influence of Shield Tunneling Crossing underneath Intercity Railway and Shield Tunneling Parameters Optimization. *Advances in Civil and Industrial Engineering, Pts 1-4*, 353-356:1619-1624. <https://doi.org/10.4028/www.scientific.net/AMM.353-356.1619>
- Dige N and Diwekar U, 2018. Efficient sampling algorithm for large-scale optimization under uncertainty problems. *Computers & Chemical Engineering*, 115:431-454. <https://doi.org/10.1016/j.compchemeng.2018.05.007>
- Ding LY, Wang F, Luo HB, et al., 2013. Feedforward Analysis for Shield-Ground System. *Journal of Computing in Civil Engineering*, 27(3):231-242. [https://doi.org/10.1061/\(Asce\)Cp.1943-5487.0000219](https://doi.org/10.1061/(Asce)Cp.1943-5487.0000219)
- Dong M, Guan MZ, Wang KH, et al., 2025. Machine

- Learning-Based Measurement and Prediction of Ground Settlement Induced by Shield Tunneling Undercrossing Existing Tunnels in Composite Strata. *Sensors*, 25(5).  
<https://doi.org/10.3390/s25051600>
- Galera JM, Pescador S, Rodriguez A, et al., 2007. Galera, J. M., Pescador, S., Rodríguez, Á., & Torres, M. (2007). Prediction of the ground conditions ahead the TBM face in the tunnels of guadarrama (spain), using geophysical methods and in situ testing. *Underground Space - the 4th Dimension of Metropolises, Vols 1-3*:203-208.  
<https://doi.org/10.1201/noe0415408073.ch33>
- Gao MT, Yang WF, Liu ZY, et al., 2024. LSTM goaf surface subsidence prediction method combining convolutional neural network and attention mechanism. *Bulletin of Surveying and Mapping*, 0(6):53-58,170.  
<https://doi.org/10.13474/j.cnki.11-2246.2024.0610>
- Ghaboussi J and Ranken RE, 1977. Interaction between two parallel tunnels. *International Journal for Numerical and Analytical Methods in Geomechanics*, 1(1):75-103.  
<https://doi.org/10.1002/nag.1610010107>
- Hage Chehade F and Shahrour I, 2008. Numerical analysis of the interaction between twin-tunnels: Influence of the relative position and construction procedure. *Tunnelling and Underground Space Technology*, 23(2):210-214.  
<https://doi.org/10.1016/j.tust.2007.03.004>
- Herrenknecht, 2024. Pioneering Underground Together.
- Hia S, Kuswanto H and Prastyo DD, 2023. Robustness of Support Vector Regression and Random Forest Models: A Simulation Study. *Data Science and Emerging Technologies*, Singapore. Springer Nature Singapore, p. 465-479.
- Hou GY, Xu ZD, Li L, et al., 2020. Shield Tunneling Parameter Matching Model and UI Interface. *Advances in Civil Engineering*, 2020:9562828.  
<https://doi.org/10.1155/2020/9562828>
- Hou YJ, Zhou MZ, Zhang DL, et al., 2022. Analysis of four shield-driven tunnels with complex spatial relations in a clay stratum. *Tunnelling and Underground Space Technology*, 124:104478.  
<https://doi.org/10.1016/j.tust.2022.104478>
- Hu XY, Cheng JG and Ju JW, 2021. Influence of the Cutterhead Configuration and Operation Parameters on the Face Stability of EPB Shield Tunnels in Dry Granular Soils. *International Journal of Geomechanics*, 21(5):04021050.  
[https://doi.org/10.1061/\(ASCE\)GM.1943-5622.0002008](https://doi.org/10.1061/(ASCE)GM.1943-5622.0002008)
- Huang HW, Chang JQ, Zhang DM, et al., 2022. Machine learning-based automatic control of tunneling posture of shield machine. *Journal of Rock Mechanics and Geotechnical Engineering*, 14(4):1153-1164.  
<https://doi.org/10.1016/j.jrmge.2022.06.001>
- Huang K, Sun YW, Zhou DQ, et al., 2021. Influence of water-rich tunnel by shield tunneling on existing bridge pile foundation in layered soils. *Journal of Central South University*, 28(8):2574-2588.  
<https://doi.org/10.1007/s11771-021-4787-6>
- Kim CY, Bae GJ, Hong SW, et al., 2001. Neural network based prediction of ground surface settlements due to tunnelling. *Computers and Geotechnics*, 28(6-7):517-547.  
[https://doi.org/10.1016/S0266-352x\(01\)00011-8](https://doi.org/10.1016/S0266-352x(01)00011-8)
- Kong FC, Lu DC, Ma YD, et al., 2022. Analysis and Intelligent Prediction for Displacement of Stratum and Tunnel Lining by Shield Tunnel Excavation in Complex Geological Conditions: A Case Study. *Ieee Transactions on Intelligent Transportation Systems*, 23(11):22206-22216.  
<https://doi.org/10.1109/Tits.2022.3149819>
- Li C, Li JH, Shi ZQ, et al., 2022. Prediction of Surface Settlement Induced by Large-Diameter Shield Tunneling Based on Machine-Learning Algorithms. *Geofluids*, 2022:4174768.  
<https://doi.org/10.1155/2022/4174768>
- Li JH, Li PX, Guo D, et al., 2021. Advanced prediction of tunnel boring machine performance based on big data. *Geoscience Frontiers*, 12(1):331-338.  
<https://doi.org/10.1016/j.gsf.2020.02.011>
- Li JP, Huang HX and Wang G, 2025. A Small-Sample Prediction Model for Ground Surface Settlement in Shield Tunneling Based on Adjacent-Ring Graph Convolutional Networks (GCN-SSPM). *Buildings*, 15(19).  
<https://doi.org/10.3390/buildings15193519>
- Li ZC, Chen RP, Meng FY, et al., 2015. Tunnel boring machine tunneling-induced ground settlements in soft clay and influence of excavation parameters. *Journal of Zhejiang University (Engineering Science)*, 49(7):1268-1275.  
<https://doi.org/10.3785/j.issn.1008-973X.2015.07.010>
- Lin CJ, Yang XD, Gong YJ, et al., 2021. Prediction Model of In-chamber Earth Pressure for EPB Shield Based on PSO-BP and Parameter Sensitivity Analysis of Tunneling Parameters. *Journal of Basic Science and Engineering*, 29(5):1220-1233.  
<https://doi.org/10.16058/j.issn.1005-0930.2021.05.011>
- Liu WL and Ding LY, 2020. Global sensitivity analysis of influential parameters for excavation stability of metro tunnel. *Automation in Construction*, 113:103080.  
<https://doi.org/10.1016/j.autcon.2020.103080>
- Luo ZJ, Li Z, Tan JZ, et al., 2020. Three-dimensional fluid-soil full coupling numerical simulation of ground settlement caused by shield tunnelling. *European Journal of Environmental and Civil Engineering*, 24(8):1261-1275.  
<https://doi.org/10.1080/19648189.2018.1464961>
- Lv JB, Li XL, Fu HL, et al., 2020. Influence of shield tunnel construction on ground surface settlement under the condition of upper-soft and lower-hard composite strata. *Journal of Vibroengineering*, 22(5):1126-1144.  
<https://doi.org/10.21595/jve.2020.20967>
- Mair RJ, Taylor RN and Bracegirdle A, 1993. Subsurface settlement profiles above tunnels in clays. *Géotechnique*, 43(2):315-320.  
<https://doi.org/10.1680/geot.1993.43.2.315>

- Maleki MR, 2018. Rock Joint Rate (RJR); a new method for performance prediction of tunnel boring machines (TBMs) in hard rocks. *Tunnelling and Underground Space Technology*, 73:261-286.  
<https://doi.org/10.1016/j.tust.2017.12.022>
- Niu YL, Ren TL, Zhou Q, et al., 2023. Analysis of Excavation Parameters on Face Stability in Small Curvature Shield Tunnels. *Sustainability*, 15(8):6797.  
<https://doi.org/10.3390/su15086797>
- Pourtaghi A and Lotfollahi-Yaghin MA, 2012. Wavenet ability assessment in comparison to ANN for predicting the maximum surface settlement caused by tunneling. *Tunnelling and Underground Space Technology*, 28:257-271.  
<https://doi.org/10.1016/j.tust.2011.11.008>
- Rashid TA, Fattah P and Awla DK, 2018. Using Accuracy Measure for Improving the Training of LSTM with Metaheuristic Algorithms. *Cyber Physical Systems and Deep Learning*, 140:324-333.  
<https://doi.org/10.1016/j.procs.2018.10.307>
- Richa T, Lebdaoui S, Pereira JM, et al., 2023. A Comparative Study of Ensemble Methods for Prediction of Surface Settlement Induced by TBM Tunneling. *Geo-Risk 2023: Innovation in Data and Analysis Methods*, 345:211-219.  
<https://doi.org/10.1061/9780784484975.023>
- Shen ZW, Yang HZ and Zhang SJ, 2021. Neural network approximation: Three hidden layers are enough. *Neural Networks*, 141:160-173.  
<https://doi.org/10.1016/j.neunet.2021.04.011>
- Shi G, Qin CJ, Tao JF, et al., 2021. A VMD-EWT-LSTM-based multi-step prediction approach for shield tunneling machine cutterhead torque. *Knowledge-Based Systems*, 228:107213.  
<https://doi.org/10.1016/j.knosys.2021.107213>
- Sobol IM, 2001. Global sensitivity indices for nonlinear mathematical models and their Monte Carlo estimates. *Mathematics and Computers in Simulation*, 55(1-3):271-280.  
[https://doi.org/10.1016/S0378-4754\(00\)00270-6](https://doi.org/10.1016/S0378-4754(00)00270-6)
- Song MY, Yang MH, Yao GZ, et al., 2024. Artificial intelligence driven tunneling-induced surface settlement prediction. *Automation in Construction*, 168.  
<https://doi.org/10.1016/j.autcon.2024.105819>
- Standing JR and Burland JB, 2006. Unexpected tunnelling volume losses in the Westminster area, London. *Géotechnique*, 56(1):11-26.  
<https://doi.org/10.1680/geot.2006.56.1.11>
- Sun SL, 2022. Shield Tunneling Parameters Matching Based on Support Vector Machine and Improved Particle Swarm Optimization. *Scientific Programming*, 2022:6782947.  
<https://doi.org/10.1155/2022/6782947>
- Suwansawat S and Einstein HH, 2006. Artificial neural networks for predicting the maximum surface settlement caused by EPB shield tunneling. *Tunnelling and Underground Space Technology*, 21(2):133-150.  
<https://doi.org/10.1016/j.tust.2005.06.007>
- Taylor KE, 2001. Summarizing multiple aspects of model performance in a single diagram. *Journal of Geophysical Research-Atmospheres*, 106(D7):7183-7192.  
<https://doi.org/10.1029/2000jd900719>
- Tsai MY and Cho HH, 2021. Differential-evolution-based weights fine tuning mechanism for GRU to predict 5G traffic flow. 2021 International Symposium on Intelligent Signal Processing and Communication Systems (ISPACS), Hualien. IEEE, p. 1-2.  
<https://doi.org/10.1109/ISPACS51563.2021.9650923>
- Wang L, Pan QJ and Wang SY, 2024. Data-driven predictions of shield attitudes using Bayesian machine learning. *Computers and Geotechnics*, 166:106002.  
<https://doi.org/10.1016/j.compgeo.2023.106002>
- Wang LY, Que HB and Wu F, 2025. The CNN-LSTM-attention model for short term prediction of the polar motion. *Measurement Science and Technology*, 36(1):016323.  
<https://doi.org/10.1088/1361-6501/ad8be5>
- Wang RH, Li DQ, Chen EJ, et al., 2021. Dynamic prediction of mechanized shield tunneling performance. *Automation in Construction*, 132:103958.  
<https://doi.org/10.1016/j.autcon.2021.103958>
- Wei HB, Wei DS, Jiang BY, et al., 2023. Prediction Analysis of Settlement of Existing Road Under Shield Tunneling Based on IPSO-SVR. *Journal of South China University of Technology (Natural Science)*, 51(6):62-71.  
<https://doi.org/10.12141/j.issn.1000-565X.220553>
- Wu B, Xu J, Huang W, et al., 2019. Prediction of ground settlement on shielded water-rich sand layer considering groundwater level and tunnel depth. *5th International Conference on Advances in Energy, Environment and Chemical Engineering*, 358:042045.  
<https://doi.org/10.1088/1755-1315/358/4/042045>
- Xu YJ and Chen XS, 2023. Current Situation and Prospect of Comprehensive Development of Underground Space in Metro Area. *Chinese Journal of Underground Space and Engineering*, 19(1):1-12.  
<https://doi.org/10.20174/j.juse.2023.01.001>
- Yang MH, Song MY, Guo YW, et al., 2025. Prediction of shield tunneling-induced ground settlement using LSTM architecture enhanced by multi-head self-attention mechanism. *Tunnelling and Underground Space Technology*, 161:106536.  
<https://doi.org/10.1016/j.tust.2025.106536>
- Ye XW, Zhang XL, Zhang HQ, et al., 2023. Prediction of lining upward movement during shield tunneling using machine learning algorithms and field monitoring data. *Transportation Geotechnics*, 41.  
<https://doi.org/10.1016/j.trgeo.2023.101002>
- Zhang N, Zhang N, Zheng Q, et al., 2022. Real-time prediction of shield moving trajectory during tunnelling using GRU deep neural network. *Acta Geotechnica*, 17(4):1167-1182.  
<https://doi.org/10.1007/s11440-021-01319-1>
- Zhang P, Chen RP and Wu HN, 2019. Real-time analysis and regulation of EPB shield steering using Random Forest.

*Automation in Construction*, 106:102860.

<https://doi.org/10.1016/j.autcon.2019.102860>

Zhang P, Chen RP, Wu HN, et al., 2020a. Ground settlement induced by tunneling crossing interface of water-bearing mixed ground: A lesson from Changsha, China. *Tunnelling and Underground Space Technology*, 96:103224.

<https://doi.org/10.1016/j.tust.2019.103224>

Zhang P, Wu HN, Chen RP, et al., 2020b. A critical evaluation of machine learning and deep learning in shield-ground interaction prediction. *Tunnelling and Underground Space Technology*, 106:103593.

<https://doi.org/10.1016/j.tust.2020.103593>

Zhang P, Yin ZY, Jin YF, et al., 2020c. A novel hybrid surrogate intelligent model for creep index prediction based on particle swarm optimization and random forest. *Engineering Geology*, 265:105328.

<https://doi.org/10.1016/j.enggeo.2019.105328>

Zhang WG, Li HR, Wu CZ, et al., 2021a. Soft computing approach for prediction of surface settlement induced by earth pressure balance shield tunneling. *Underground Space*, 6(4):353-363.

<https://doi.org/10.1016/j.undsp.2019.12.003>

Zhang YQ, Cao WG, Zhou SH, et al., 2021b. Prediction of three-dimensional subface and subsurface settlement caused by shield tunnelling based on Peck formula. *Journal of Railway Science and Engineering*, 18(1):153-161.

<https://doi.org/10.19713/j.cnki.43-1423/u.T20200181>

Zhao J, Yang WC and Zhu F, 2024. A CNN-LSTM-Attention Model for Near-Crash Event Identification on Mountainous Roads. *Applied Sciences-Basel*, 14(11):4934.

<https://doi.org/10.3390/app14114934>

Zhou XZ, Zhao C and Bian XC, 2023a. Prediction of maximum ground surface settlement induced by shield tunneling using XGBoost algorithm with golden-sine seagull optimization. *Computers and Geotechnics*, 154:105156.

<https://doi.org/10.1016/j.compgeo.2022.105156>

Zhou Z, Zhang JJ, Ding HH, et al., 2023b. Settlement prediction model of shield tunnel under-crossing existing tunnel based on GA-Bi-LSTM. *Chinese Journal of Rock Mechanics and Engineering*, 42(1):224-234.

<https://doi.org/10.13722/j.cnki.jrme.2021.1187>

## Electronic supplementary materials

Sections S1-S5, Tables S1 and S2, Figs. S1-S12, Appendix A and B.

## 中文概要

题目：盾构隧道施工地表沉降预控的 EPB 运行参数自

## 适应调整策略：案例研究

**目的：**盾构隧道施工过程中，地表变形对周边建（构）筑物和地下管线安全构成威胁。现有全参数优化策略忽略了盾构运行参数间的交互耦合关系，导致理论优化结果与实际施工存在偏差，预控效果不佳。本文旨在提出一种融合优化与反演的盾构运行参数自适应调整策略，通过区分参数的可控性与敏感性，在有效降低地表沉降的同时保持参数间的固有协同关系，实现土压平衡盾构施工地表沉降的主动预控。

**创新点：**1. 提出了一种融合优化搜索与反演预测的复合机制，通过对盾构运行参数进行多级分类，在降低地表沉降的同时最大限度保留参数间交互关系；2. 构建了融合多头自注意力机制的双向长短期记忆网络模型（MHSA-Bi-LSTM），有效捕捉盾构施工沉降数据的时空序列依赖关系，提高了沉降预测精度。

**方法：**1. 以长春地铁 6 号线飞跃广场站-欧亚卖场站盾构隧道工程为依托，融合地质参数、盾构运行参数及地表沉降监测数据，构建多源异构数据集（图 10）；2. 建立 MHSA-Bi-LSTM 沉降预测元模型（模型 1），与 SVR、RF、Transformer、Bi-LSTM 模型对比验证其预测优越性；3. 基于 Sobol 全局敏感性分析方法，识别出对地表沉降影响显著的运行参数（ $V_E$ 、 $P_S$ 、 $R_C$ 、 $T_C$ ），采用 PSO 算法对高敏感度参数（Category A）进行优化搜索（图 15 和 16）；4. 采用随机森林算法构建反演模型（模型 2 和 3），对低敏感度不可控参数（Category B： $T_T$ 、 $T_{SC}$ 、 $V_G$ ）和可控参数（Category C： $R_{SC}$ 、 $S_A$ ）进行层级反演预测（图 18 和 19）；5. 在后施施工环号（715-910 环）进行现场验证，对比自适应调整策略与全参数优化策略的实际预控效果（图 22 和 24）。

**结论：**1. MHSA-Bi-LSTM 模型相较于 Bi-LSTM、Transformer、RF 和 SVR 模型具有更优的沉降预测性能，其增强的记忆保持能力和多头自注意力机制能有效捕捉盾构施工数据中的时空依赖关系；2. Sobol 全局敏感性分析表明，开挖土方量（ $V_E$ ）、支护压力（ $P_S$ ）、刀盘转速（ $R_C$ ）和刀盘扭矩（ $T_C$ ）对地表沉降影响显著，在一定范围内降低  $V_E$ 、 $R_C$ 、 $T_C$  并提高  $P_S$  可有效减小地表沉降；3. 针对有限监测精度场景，随机森林反演模型相较于 SVR 模型，测试集 MAE 和 RMSE 分别平均降低 27.46% 和 27.03%；4. 全参数优化策略导致不可控参数平均偏离理论目标值土

34.27%，而自适应调整策略将不可控参数平均波动控制在 $\pm 13.95\%$ 以内，参数变化趋势与可控参数优化方向呈现显著协同性；5. 现场验证表明，与基准平均沉降 6.15 mm（170-665 环，未优化）相比，全参数优化策略和自适应调整策略的平均沉降分别为 4.72 mm 和 3.81 mm，分别改善 23.25% 和 38.05%，后者预控效果显著优于前者。

**关键词：**沉降预控；优化与反演；多头自注意力机制；长短期记忆网络；随机森林算法；盾构隧道

Unedited